nature physics

Article

https://doi.org/10.1038/s41567-026-03392-3

Superconductivity under pressure in a van der Waals heavy-fermion metal

Received: 9 September 2025

Accepted: 26 June 2026

Published online: 28 July 2026

Check for updates

Tong Shi[1,2,8], Wenhao Li[3,4,8], Qingxin Dong[1,5,8], Pengtao Yang[1,5], Hanming Ma[1,5], Zhaoming Tian[2], Ningning Wang[1,5], Jianping Sun[1,5], Yoshiya Uwatoko[6,7], Yi-feng Yang[1,5] ✉, Bosen Wang[1,5] ✉, Hechang Lei[3,4] ✉ & Jinguang Cheng[1,5] ✉

CeSiI is a van der Waals heavy-fermion metal featuring a long-range antiferromagnetic order and Kondo coherence. The phase diagram that details the evolutions of the transition temperatures of those two orders as a function of external tuning parameters such as pressure is crucial for understanding strong electron interactions in heavy-fermion systems. Here we experimentally demonstrate the phase diagram of CeSiI. The critical temperature of the Kondo coherent state exhibits a V-shaped, non-monotonic dependence on pressure. Upon suppression of the antiferromagnetic order, a superconducting dome emerges with a maximum transition temperature of about 240 mK and the coherence temperature reaches its minimum. The close proximity of superconductivity to antiferromagnetic instability, together with a large upper critical field, suggests an unconventional pairing mechanism in CeSiI. Normal-state transport measurements further provide evidence for quantum criticality, as manifested by non-Fermi-liquid behaviour and divergence of the effective electron mass. Our findings support CeSiI as a heavy-fermion superconductor and reveal an unconventional nature for its Kondo coherence at ambient pressure, thus offering a platform for exploring the interplay among strong electron correlations, Kondo hybridization, magnetism and unconventional superconductivity in two-dimensional heavy-fermion systems.

Exfoliable two-dimensional (2D) van der Waals (vdW) quantum materials have attracted increasing research interest for exploring dimensionality-driven physical phenomena and fabrication of nano-electronic devices[1–9]. The prototype examples include graphene[1,2], black phosphorus[3,4], transition-metal dichalcogenides[5,6] and potential monolayer ferromagnets such as CrI_3 and Fe_3GeTe_2 (refs. 7–9). The recent discovery of CeSiI has expanded the vdW quantum materials to heavy-fermion systems, which are characterized by the inheritance of strong electron correlations[10]. As shown in Fig. 1a,b, CeSiI adopts a layered hexagonal structure with a trigonal *P*-3*m*1 space group. Each block of CeSiI consists of an almost flat honeycomb lattice of Si atoms in the middle, connected to a triangular layer of Ce atoms on both sides, and then covered by iodine atoms at the outermost layers[10,11]. These CeSiI blocks are stacked alternatively along the *c* axis via weak vdW interactions, facilitating exfoliations of CeSiI flakes down to few-layer limit[10,12]. Previous studies conducted at ambient pressure (AP) have established bulk CeSiI as a vdW heavy-fermion metal with two characteristic transitions upon decreasing temperature, that is, the formation

[1]Beijing National Laboratory for Condensed Matter Physics and Institute of Physics, Chinese Academy of Sciences, Beijing, China. [2]Wuhan National High Magnetic Field Center and School of Physics, Huazhong University of Science and Technology, Wuhan, China. [3]Department of Physics, Beijing Key Laboratory of Optoelectronic Functional Materials and Micro-Nano Devices, Renmin University of China, Beijing, China. [4]Key Laboratory of Quantum State Construction and Manipulation (Ministry of Education), Renmin University of China, Beijing, China. [5]School of Physical Sciences, University of Chinese Academy of Sciences, Beijing, China. [6]Department of Advanced Materials Science, Graduate School of Frontier Sciences, University of Tokyo, Chiba, Japan. [7]Department of Natural Sciences, Faculty of Science and Engineering, Tokyo City University, Tokyo, Japan. [8]These authors contributed equally: Tong Shi, Wenhao Li, Qingxin Dong. ✉e-mail: yifeng@iphy.ac.cn; bswang@iphy.ac.cn; hlei@ruc.edu.cn; jgcheng@iphy.ac.cn

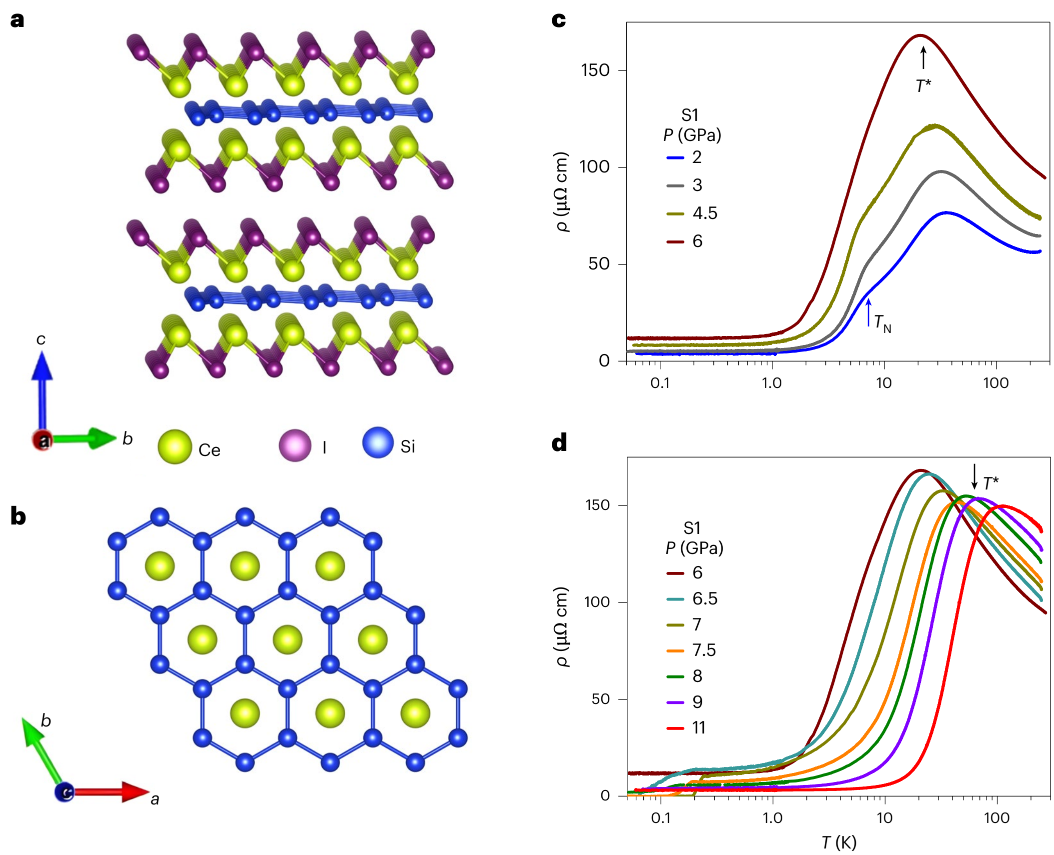

Fig. 1 | Crystal structure and high-pressure resistivity of CeSiI. a,**b**, Crystal structures of CeSiI from side (**a**) and top (**b**) views. **c**,**d**, The $\rho(T)$ of CeSiI (S1) under various pressures: 2–6 GPa (**c**) and 6–11 GPa (**d**). The black and blue arrows mark the characteristic temperatures T^* and T_N for the formation of the Kondo coherence state and the AF order, respectively.

of Kondo coherence at $T^* \approx 50$ K and an incommensurate AF order at $T_N \approx 7.5$ K. These transitions are manifested by a broad shoulder and a pronounced drop in resistivity $\rho(T)$, respectively[10,11]. In the recent study, the emergence of coherent hybridization of Ce-4*f* and conduction electrons at low temperatures was supported by the angle-resolved photoemission spectroscopy and scanning tunnelling microscopy measurements[10]. However, the full recovery of magnetic doublet entropy Rln2 up to 20 K (<<T^*) and well retention of Curie–Weiss behaviour across T^* are inconsistent with the conventional scenario of Kondo coherent state formation at T^*(ref. 10). This issue is critical as it lays the basis for further exploration of potential topological properties of the material[10,12,13]. Moreover, theoretical calculations on CeSiI have highlighted strain-sensitive Kondo hybridization and Ruderman–Kittle–Kasuya–Yosida interaction, positioning it as a prototypical platform for exploring 2D quantum criticality[14]. Preliminary high-pressure measurements up to 1.6 GPa have shown a downward shift of T^* and T_N, but the pressure and temperature ranges are far from an AF quantum critical point (QCP)[10,14] in the Kondo-magnetic phase diagram[10,12]. It is thus imperative to extend it further towards the QCP and to explore the relation of the Kondo coherent state and the AF order, as well as possible unconventional superconductivity[10,12,15–18]. Here, we are motivated to determine the complete evolutions of T^* and T_N as a function of external pressure (P) aiming to clarify the unconventional nature of Kondo states and to explore exotic phenomena driven by quantum criticality in CeSiI.

Pressure evolutions of T^* and T_N

Figure 1c,d shows the temperature dependence of resistivity, $\rho(T)$, in a semi-logarithmic scale for a CeSiI single crystal (S1) under various hydrostatic pressures from 2 to 11 GPa down to 50 mK. As seen in Fig. 1c, $\rho(T)$ at 2 GPa is featured by a broad hump at $T^* \approx 36$ K and a kink-like anomaly at $T_N \approx 5$ K, which are lowered in comparison with those at AP[10,11] (Extended Data Fig. 1). It is noted that the shoulder anomaly around T^* at AP is enhanced gradually by pressure and changes into a pronounced hump with increasing pressure. Here the values of T_N and T^* are defined as the points where dρ/dT peaks out and crosses zero, respectively (Extended Data Fig. 2). As pressure is applied gradually to 6 GPa, the magnitude of $\rho(T)$ increases monotonically over the entire temperature range, more than doubled at T^*, and both anomalies at T_N and T^* are shifted down to lower temperatures continuously, reaching about 3 K and 21 K at 6 GPa (Fig. 1c). Such a concomitant reduction of T_N and T^* at $P \leq 6$ GPa cannot be understood purely from pressure-enhanced Kondo coherence of the ground state doublet in typical Ce-based heavy-fermion compounds[16,18–20], but requires a more intricate mechanism possibly involving crystal field or spin scattering effect[11,12,21,22].

Upon further increasing pressure above 6 GPa (Fig. 1d), the evolution of $\rho(T)$ around T^* is reversed, with its magnitude reduced and T^* shifted to higher temperature progressively, increasing up to 110 K at 11 GPa. Meanwhile, the anomaly of $\rho(T)$ at T_N can be hardly defined in the low-temperature region, signalling the complete suppression of AF order at about 6 GPa. These results indicate that the enhancement of Kondo coherence occurs after the low-temperature AF order vanishes. In addition, we observed a sudden drop of resistivity at pressures above 6 GPa due to the emergence of superconductivity as described below.

The above results are reproduced on another sample CeSiI (S2) measured up to 14 GPa (Extended Data Fig. 3), that is, its T^* initially decreases to a minimum value of ~20.3 K at 5.5 GPa and then increases monotonically up to about 300 K at 14 GPa, while its T_N is continuously suppressed to 2.85 K at 5.5 GPa. Besides these similar major features, slight sample-dependent behaviours were noticed for these samples,

 https://doi.org/10.1038/s41567-026-03392-3

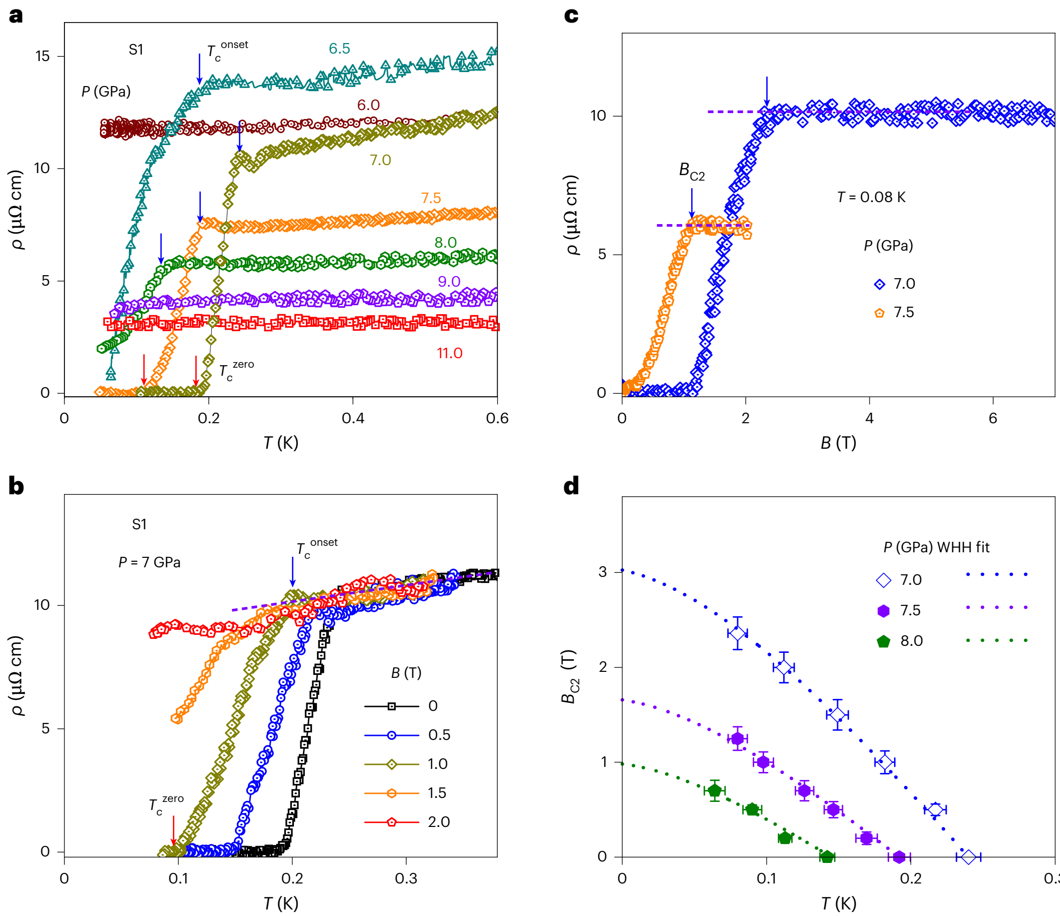

Fig. 2 | Superconducting properties of CeSiI. a, Low-T $\rho(T)$ of CeSiI (S1) under various pressures from 6 to 11 GPa and temperatures down to 0.05 K. **b**, Low-T $\rho(T)$ of CeSiI (S1) under different magnetic fields at 7 GPa; the dashed line represents the linear extension of normal-state resistivity. **c**, The $\rho(B)$ at 0.08 K for 7 and 7.5 GPa. **d**, The $B_{c2}(T)$ and corresponding fitting curves using the WHH model marked by the dashed lines. In **a** and **b**, the blue and red arrows mark the onset and zero-resistivity superconducting temperatures, T_c^{onset} and T_c^{zero}, which are defined as the temperatures where $\rho(T)$ starts to deviate from the extrapolated normal-state behaviour and reaches zero, respectively. In **d**, we choose T_c^{onset} to mark the superconducting transition and plot the $B_{c2}(T)$ and the error bars represent the uncertainty in determining T_c.

such as the magnitude of $\rho(T)$ around T^* and the residual resistivity ratio, RRR ≡ $\rho(T^*)/\rho(1.6\text{ K})$, which are 7.9 (7.4) for S1 (S3) and 1.5 for S2 at AP (Extended Data Fig. 1b). The relatively large RRR value of S1, which is almost two times those (4.3) in refs. 10,11, confirms the high-quality of CeSiI crystals used in the present study. We thus focus on this sample in the present study.

Emergence of superconductivity

The emergence of superconductivity upon suppression of AF order above about 6 GPa and its evolution with pressure can be seen in Fig. 2a. At 6.5 GPa, $\rho(T)$ starts to drop from about 0.2 K, signalling the onset of superconducting transition, but zero resistance cannot be achieved down to 0.05 K. By increasing pressure to 7 GPa, the superconducting transition becomes sharper and moves to higher temperatures with $T_c^{onset} \approx 0.24$ K and $T_c^{zero} \approx 0.19$ K, which are defined as the temperatures where $\rho(T)$ starts to deviate from the extrapolated normal-state behaviour and reaches zero, respectively (Fig. 2a). The superconducting transition is quickly suppressed upon further applying pressure and becomes undetectable down to 0.05 K at 11 GPa. This indicates that pressure-induced superconductivity in CeSiI exists in a quite narrow pressure range of 6–9 GPa.

The occurrence of superconductivity is reproducible on sample S2 measured in a dilution refrigerator during the decompression process, showing the emergence of superconductivity with $T_c^{onset} \approx 0.14$ K at 5.9 GPa, reaching the maximum of about 0.25 K at 6.6 GPa, and then decreasing to about 0.15 K at 7.9 GPa (Extended Data Fig. 4a,b). For this sample, zero resistivity was not reached, presumably due to the residual strain upon decompression from 14 GPa and/or the relatively low sample quality (for example, disorder and non-stoichiometry) with a smaller RRR value shown above.

To gain further insights into the superconducting properties of CeSiI, we studied the effect of magnetic field, B, on the superconducting transition by measuring low-T $\rho(T)$ under various magnetic fields at $P = 7$, 7.5 and 8 GPa (Fig. 2b and Extended Data Fig. 5) and $\rho(B)$ at 0.08 K at 7 and 7.5 GPa (Fig. 2c). As can be seen, the superconducting transition is shifted gradually to lower temperatures with increasing B, and the upper critical field, B_{c2}, at 0.08 K decreases from 2.4 T at 7 GPa to 1.2 T at 7.5 GPa. To quantify the evolution of zero-temperature upper critical field $B_{c2}(0)$ under pressure, we chose T_c^{onset} to mark the superconducting transition and plot the temperature dependence of $B_{c2}(T)$ in Fig. 2d, which can be well described by using the Werthamer–Helfand–Hohenberg (WHH) model[23]. The best fits, shown by the dashed lines, yield $B_{c2}(0) \approx 3.03$, 1.66 and 0.98 T for 7, 7.5 and 8 GPa, respectively. These values are about four to seven times the Pauli paramagnetic limit $B_p = 1.84T_c$, implying an unconventional nature for the observed superconductivity as discussed below.

T–*P* phase diagram

Based on the above results, we construct the T–P phase diagram of CeSiI (Fig. 3), which reveals a concomitant evolution of $T^*(P)$ and

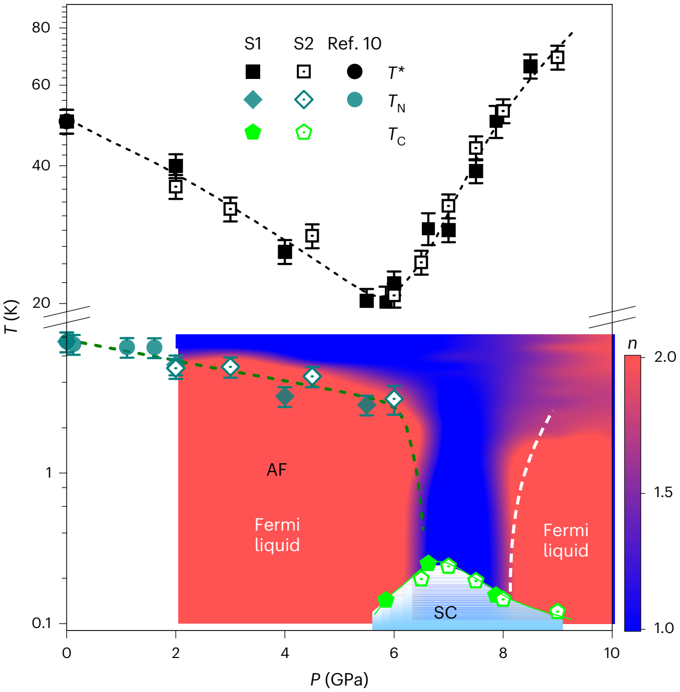

Fig. 3 | Temperature–pressure phase diagram of CeSiI. Pressure dependence of the Kondo coherence temperature T^*, AF transition temperature T_N and superconducting transition temperature T_c. The characteristic temperatures of CeSiI from ref. 10 are included for comparison. The colour contour plot of the exponent $n(T, P)$ was superimposed on the T–P diagram highlighting the crossovers from Fermi-liquid to non-Fermi-liquid behaviours. The dashed white points indicate the Fermi liquid boundary. The error bars represent the uncertainties in determining these characteristic temperatures.

$T_N(P)$ as well as the dome-shaped $T_c(P)$. With increasing pressure, both $T^*(P)$ and $T_N(P)$ are initially reduced concurrently: $T^*(P)$ reaches a minimum of 20 K at about 6 GPa and then increases quickly with pressure, while $T_N(P)$ vanishes at the same pressure, signalling the occurrence of pressure-driven AF instability[15,18–20]. Meanwhile, a dome-like superconducting $T_c(P)$ with a maximum of 0.24 K at about 7 GPa emerges in a narrow pressure range of 6–9 GPa. As shown below, the superconducting dome is developed from a non-Fermi-liquid normal state sandwiched by Fermi-liquid phases on both sides in the T–P phase diagram.

While the emergence of superconductivity around the AF QCP closely resembles many other heavy-fermion superconductors and implies an unconventional pairing mechanism[15–18], the unusual non-monotonic evolution of $T^*(P)$ differs from most Ce-based heavy-fermion materials[16,19,20]. Rather, the overall phase diagram is reminiscent of pressurized $CeRhIn_5$ (ref. 24), where the initial decrease of $T^*(P)$ has been ascribed to some effects associated with AF spin fluctuations[25] while the f-electrons remain localized in this regime[26,27]. Such a scenario seems to be inconsistent with previous scanning tunnelling microscopy and angle-resolved photoemission spectroscopy observations of the Kondo coherent state below T^* at AP for CeSiI (ref. 10). A closer inspection of specific heat and magnetic susceptibility measurements suggests that the f-electrons are indeed localized deep below T^* in CeSiI at AP, because the magnetic entropy is fully recovered at about 20 K (ref. 10) and the magnetic susceptibility grows continuously across T^* following the Curie–Weiss behaviour (Extended Data Fig. 1c), with an effective moment $\mu_{eff} = 2.47(1)\,\mu_B$ per f.u. close to the effective moment of free Ce^{3+} ions[11,15]. Moreover, only light carriers with effective masses comparable to that of a bare electron are observed via the SdH measurements[10]. These experimental facts together with the similar $T^*(P)$ between CeSiI and $CeRhIn_5$ strongly suggest that the Kondo coherent state around T^* cannot be understood simply from the Kondo coherence of the Ce-4f ground state doublet but requires more studies.

Evidence of quantum criticality

To gain further insight into the AF QCP of CeSiI, we performed quantitative analyses on the resistivity just above T_c by using the power-law formula, viz., $\rho(T) = \rho_0 + AT^n$, where ρ_0 is the residual resistivity. The exponent $n = 2$ indicates Fermi-liquid behaviour with the quadratic temperature coefficient A proportional to the effective mass of carriers, that is, $A \propto (m^*/m_0)^2$. We first plot the low-temperature $\rho(T)$ data in the form of ρ versus T^2 (Fig. 4a and Extended Data Fig. 6b), from which the quadratic-temperature coefficient A can be extracted as the initial slope of a linear fitting to each curve while the intercept gives ρ_0.

Figure 4b,c displays the pressure dependencies of ρ_0 and A, both of which exhibit divergent behaviours around $P_c \approx 7$ GPa, where the superconducting dome reaches the maximum. Notably, the quadratic coefficient $A(P)$ is enhanced by more than an order of magnitude from 2 GPa to P_c, and then it is reduced quickly to nearly zero at $P \geq 9$ GPa. Such divergent behaviour near P_c can be described by a power-law fitting to $A(P) \propto (P - P_c)^{-\beta}$, which yields $\beta^- \approx 0.5$ and $P_c^- \approx 6.71$ GPa for $P < P_c$ and $\beta^+ \approx 1.25$ and $P_c^+ \approx 6.57$ GPa for $P > P_c$, respectively. Such critical behaviours are characteristic of quantum criticality[28,29], indicative the divergence of effective electron mass. This is further substantiated by analysing the upper critical field near P_c as $m^*/m_0 \propto [-dB_{c2}(T)/T_c dT|_{T=Tc}]^{1/2}$, which shows an enhancement to 8.5 at 7 GPa, 7.5 at 7.5 GPa and 7.9 at 8 GPa, respectively. The positive correlation between $A(P)$ and $T_c(P)$ suggests that enhanced m^* near the AF QCP due to spin fluctuations should be responsible for the dome-like superconducting diagram. Meanwhile, it is noteworthy that our fits of $A(P) \propto |P - P_c|^{-\alpha\beta}$ yield different exponents for the pressure regions below and above P_c. Such an asymmetry of $A(P)$ becomes apparent when the two sides correspond to different magnetic ground states or even Fermi surface structures[26].

As shown in Fig. 4a, a deviation from the Fermi-liquid behaviour can be clearly observed near P_c. To extract the exponent n, we performed a polynomial fitting to $\rho(T) = \rho_0 + A'T^n$ for $T_c < T < 2$ K and plotted the obtained $n(P)$ in Fig. 4d. As can be seen, the exponent n initially retains about 2 within the pressure range of 2–6 GPa, decreases to a minimum value of 1 around $P_c \approx 7$ GPa, and then recovers to about 2 above 11 GPa. The emergence of non-Fermi-liquid behaviour near P_c can be visualized in the colour contour plot of $n(T, P)$ superimposed on the T–P phase diagram in Fig. 3, which is another hallmark of quantum criticality with enhanced critical spin fluctuations near the AF QCP[18,30–34].

Such T-linear resistivity has been observed near the QCP in many heavy-fermion systems, but ascribed to different mechanisms, such as the spin-density wave in 2D or other exotic scenarios[34]. Which scenario applies to CeSiI is closely associated with the relation of the AF order and the Kondo coherent state. If the AF order originates from Fermi surface instability of the coherent heavy-fermion state, the QCP belongs to the spin-density wave type as reported for $CeCoIn_5$ (ref. 35). Meanwhile, if the f-electrons remain localized and the AF order is destroyed, accompanied by a sudden jump in the Fermi surface size, the QCP may be of the Kondo breakdown or other unconventional type, as suggested for $CeRhIn_5$ (ref. 36) and $YbRh_2Si_2$ (ref. 37). The resemblance of the T–P phase diagram between CeSiI and $CeRhIn_5$ suggests that they might belong to the same category. However, frustration might extend the QCP into a finite region with an intermediate spin-liquid-type ground state, as reported previously in the distorted kagome Kondo lattice CePdAl (ref. 38). In this regard, the frustration-driven criticality or competing exchange interactions are credible alternative explanations considering the incommensurate magnetic order and the triangular-lattice motif in CeSiI. More elaborate investigations on the Fermi surface reconstruction are necessary to establish this issue and reveal other exotic properties around the QCP, potentially arising from the interplay of the Kondo effect, magnetic frustration, superconductivity and two-dimensionality.

https://doi.org/10.1038/s41567-026-03392-3

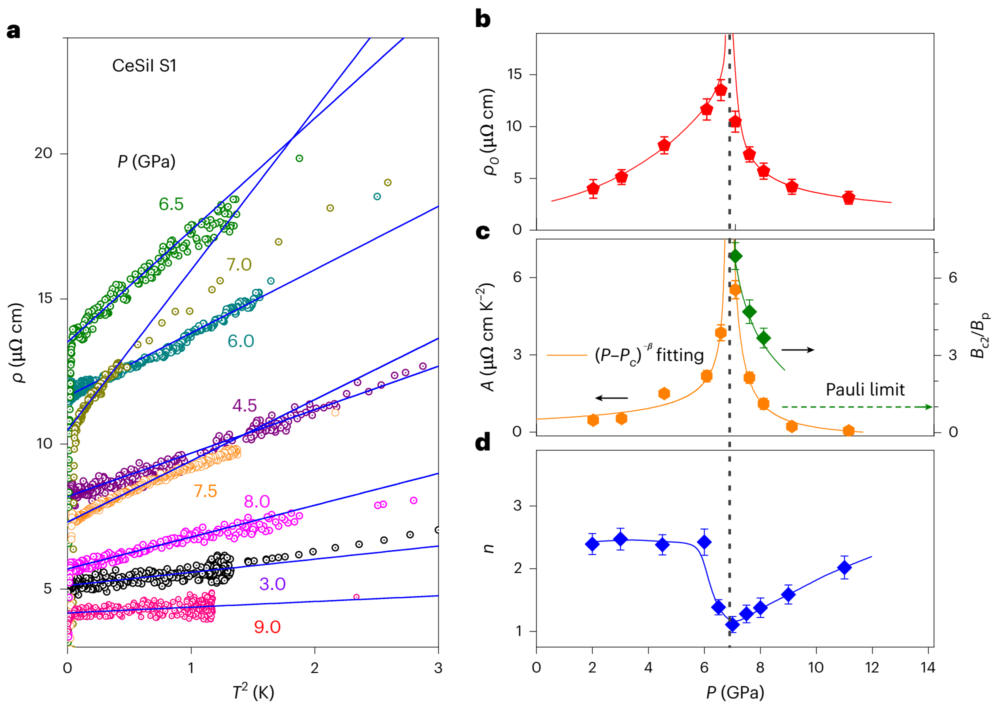

Fig. 4 | Evidence of quantum criticality. a, The ρ versus T^2 plot of low-T $\rho(T)$ data for CeSiI (S1). **b**,**c**, Pressure dependencies of the residual resistivity ρ_0 (**b**) and the quadratic-temperature coefficient A (**c**, left) and the B_{c2}/B_P (**c**, right); $A(P)$ in **c** was extracted from the linear fitting to ρ versus T^2 in **a** and fitted via $A(P) \propto (P\text{-}P_c)^{-\beta}$ shown as the solid lines. **d**, Pressure dependencies of the exponent $n(P)$. The error bars in **b**–**d** represent the standard deviations of these fitted parameters obtained from the least-square fittings as described in the main text.

Discussions

The discovery of superconductivity near the AF QCP of 2D vdW heavy-fermion metal CeSiI is important considering the following aspects. First, it enriches the family of heavy-fermion superconductors and provides a platform for studying unconventional superconducting mechanisms[18,30–34]. Second, the reduction of lattice dimensionality usually enhances quantum fluctuations near magnetic QCPs, which may be beneficial for higher T_c in heavy-fermion superconductors. On this basis, the dimensional tunability can provide useful approaches and perspectives for the exploration or study of heavy-fermion superconducting materials. Third, it has established a bridge between three-dimensional heavy-fermion and 2D quantum materials, providing an important approach for studying the emergent dimensionality-limited heavy fermion quantum states via mechanical exfoliation, stress, surface doping and so on[10,14].

We have repeated the electrical transport measurements for CeSiI (S4) (RRR ~4.3) under various pressures. We find that the evolution of T_N and T^* are basically consistent with the results for CeSiI (S1, S2). The anisotropic upper critical field $B_{c2}(0) \approx 1.58$ T determined by the WHH model for the $B//ab$ for CeSiI (S4) at 7.0 GPa is very close to the $B_{c2}(0) \approx 1.66$ T of $B//c$ at 7.5 GPa for CeSiI (S1) in Fig. 2d. The observation indicates the possible pseudo-three-dimensional superconductivity in the 2D vdW structure of CeSiI under pressure. Many theoretical studies including topological magnetism and AF Chern insulator in the monolayer CeSiI have already been proposed as the forefront[11,13,14].

Recently, Pasupathy et al. have reported that CeSiI exhibits nodal Kondo hybridization as a consequence of its low dimensionality and Ce-site local symmetry[39]. We believe that there are three main aspects to its impact on superconductivity and the AF QCP of CeSiI: first, such nodal hybridization may favour anisotropic superconducting state with an unconventional pairing mechanism and constrain conventional s-wave pairing symmetries; second, it may induce anisotropic Ruderman–Kittle–Kasuya–Yosida interaction, resulting in strong magnetic frustration and affecting the nature of the AF QCP; third, it may cause the Fermi surface collapse in a more complex manner (strongly angle dependent) near the QCP. These will possibly lead to phenomena that have not been explored before and make the AF QCP and superconductivity more intriguing. Hence, our discovery will further stimulate experimental explorations and theoretical calculations, for example, neutron diffraction to analyse magnetic structures and theoretical calculations to reveal electronic band structures and quantum critical properties.

As noted above, the observation of large $B_{c2}(0)$ that exceeds four to seven times the conventional Pauli paramagnetic limit B_P near P_c (Fig. 4c) implies an unconventional nature for the observed superconductivity, as found in some Ce-based heavy-fermion materials[40–44]. One possible origin for such a large $B_{c2}(0)$ is the reduction of the g factor, which is related to the interaction-induced mass enhancement[45], as found in $CeSb_2$ (ref. 44) and $CeCoIn_5$ (ref. 40). As discussed above, CeSiI shows an evident mass renormalization near P_c, which may lead to the high $B_{c2}(0)$. According to ref. 44, we can estimate the electronic Sommerfeld coefficient $\gamma = 0.85$ J mol^{-1} K^{-2} from the upper critical field at 7 GPa, viz., $\gamma = C|(-dB_{c2}(T)/T_c dT|_{T=T_c})|^{1/2}$, where C is prefactor 0.1 J mol^{-1}K^{-1}T$^{-1/2}$, and $dB_{c2}(T)/T_c dT|_{T=T_c} \approx 71.6$ T K^{-2} at 7 GPa. The obtained γ value at 7 GPa exhibits about seven times enhancement compared with that of 0.125 J mol^{-1} K^{-2} at AP. At the same time, we can also estimate the γ value at 7 GPa from the Kadowaki–Woods ratio, that is, $\gamma_{KW} \approx (A/R_{KW})^{0.5} \approx 0.74$ J mol^{-1} K^{-2} based on the T^2-coefficient A(7 GPa) ≈ 5.529 μΩ cm K^{-2} and the universal value $R_{KW} \approx 10$ μΩ cm mol^2 K^2 J^{-2} for many heavy-fermion compounds. As can be seen, the estimated γ values are consistent with each other, indicating its reliability. Such a huge γ value further confirms the heavy-fermion features and mass enhancement of CeSiI near the AF QCP.

Another possible reason for high $B_{c2}(0)$ is due to the strong-coupling effect, which could enhance superconducting energy gap Δ. This scenario has successfully explained the large $B_{c2}(0)$ of UBe_{13} (ref. 46). The third possibility leading to high $B_{c2}(0)$ is the mixture or transition between even-singlet and odd-triplet pairing states, as proposed in non-centrosymmetric heavy-fermion superconductors such as $CeCoGe_3$, $CeRhSi_3$ and $CeIrSi_3$, as well as $CeRh_2As_2$, which has a global inversion symmetry but locally non-centrosymmetric environment at Ce sites[42,43,47]. Similar to $CeRh_2As_2$, CeSiI is centrosymmetric but Ce atoms are located at locally non-centrosymmetric sites. Whether the strong coupling superconductivity or locally non-centrosymmetric effect exists in CeSiI is worth more detailed theoretical and experimental investigations in the future. At the same time, the orbital limiting field $B_{c2}^{orbit}(0)$ is commonly derived from the slope of the determined B–T phase boundary at T_c, which is given as $B_{c2}^{orbit}(0) = -0.73T_c dB_{c2}(T)/dT|_{T=Tc}$ in the clean limit. The relative importance of the orbital and spin-paramagnetic effects can be described by the Maki parameter $\alpha = \sqrt{2}B_{c2}^{orbit}(0)/B_P$. In this work, the estimated α are 9.63 at 7 GPa, 6.09 at 7.5 GPa and 5.13 at 8 GPa, respectively. The $\alpha >> 1$ near P_c may enable the realization of the Fulde–Ferrel–Larkin–Ovshnikov states, or stabilize non-uniform superconducting states with spatial modulation order parameters and spin polarization[23,27,45]. The present findings thus opened an avenue for studying the emergent quantum phenomena in the 2D vdW heterostructure heavy-fermion systems.

Online content

Any methods, additional references, Nature Portfolio reporting summaries, source data, extended data, supplementary information, acknowledgements, peer review information; details of author contributions and competing interests; and statements of data and code availability are available at https://doi.org/10.1038/s41567-026-03392-3.

References

1. Yankowitz, M., Ma, Q., Herrero, P. J. & LeRoy, B. J. van der Waals heterostructures combining graphene and hexagonal boron nitride. *Nat. Rev. Phys.* **1**, 112 (2019).
2. Ramires, A. & Lado, J. L. Emulating heavy fermions in twisted trilayer graphene. *Phys. Rev. Lett.* **127**, 026401 (2021).
3. Li, L. K. et al. Black phosphorus field-effect transistors. *Nat. Nanotechnol.* **9**, 372 (2014).
4. Gusmão, R., Sofer, Z. & Pumera, M. Black phosphorus rediscovered: from bulk material to monolayers. *Angew. Chem. Int. Ed.* **56**, 8052 (2017).
5. Zhao, W. et al. Gate-tunable heavy fermions in a moiré Kondo lattice. *Nature* **616**, 61 (2023).
6. Crippa, L. et al. Heavy fermions vs doped Mott physics in heterogeneous Ta-dichalcogenide bilayers. *Nat. Commun.* **15**, 1357 (2024).
7. Huang, B. et al. Layer-dependent ferromagnetism in a van der Waals crystal down to the monolayer limit. *Nature* **546**, 270 (2017).
8. Deng, Y. J. et al. Gate-tunable room-temperature ferromagnetism in two-dimensional Fe_3GeTe_2. *Nature* **563**, 94 (2018).
9. Fei, Z. Y. et al. Two-dimensional itinerant ferromagnetism in atomically thin Fe_3GeTe_2. *Nat. Mater.* **17**, 778 (2018).
10. Posey, V. A. et al. Two-dimensional heavy fermions in the van der Waals metal CeSiI. *Nature* **625**, 483 (2024).
11. Okuma, R., Ritter, C., Nilsen, G. J. & Okada, Y. Magnetic frustration in a van der Waals metal CeSiI. *Phys. Rev. Mater.* **5**, L121401 (2021).
12. Fumega, A. O. & Lado, J. L. Nature of the unconventional heavy-fermion Kondo state in monolayer CeScil. *Nano Lett.* **24**, 4272 (2024).
13. Broyles, C. et al. UOTe: Kondo-interacting topological antiferromagnet in a van der Waals lattice. *Adv. Mater.* **37**, 2414966 (2025).
14. Jang, B. G., Lee, C., Zhu, J.-X. & Shim, J. H. Exploring two-dimensional van der Waals heavy-fermion material: data mining theoretical approach. *npj 2D Mater. Appl.* **6**, 80 (2022).
15. Gegenwart, P., Si, Q. & Steglich, F. Quantum criticality in heavy-fermion metals. *Nat. Phys.* **4**, 186 (2008).
16. Park, T. et al. Hidden magnetism and quantum criticality in the heavy fermion superconductor $CeRhIn_5$. *Nature* **440**, 65 (2006).
17. Jiao, L. et al. Chiral superconductivity in heavy-fermion metal UTe_2. *Nature* **579**, 523 (2020).
18. Mathur, N. D. et al. Magnetically mediated superconductivity in heavy-fermion compounds. *Nature* **394**, 39 (1998).
19. Xie, W. et al. Heavy fermion materials and physics. *Acta Phys. Sin.* **68**, 177101 (2019).
20. Li, Y., Sheng, Y. T. & Yang, Y. F. Theoretical progress and material studies of heavy fermion superconductors. *Acta Phys. Sin.* **70**, 017402 (2021).
21. Vijayvargia, A. & Erten, O. Nematic heavy fermions and coexisting magnetic order in CeSiI. *Phys. Rev. B* **109**, L201118 (2024).
22. Zhang, K. et al. Observation of spin-momentum-layer locking in a centrosymmetric crystal. *Phys. Rev. Lett.* **127**, 126402 (2021).
23. Khim, S. et al. Pauli-limiting effects in the upper critical fields of a clean LiFeAs single crystal. *Phys. Rev. B* **84**, 104502 (2011).
24. Park, T. et al. Isotropic quantum scattering and unconventional superconductivity. *Nature* **456**, 366 (2008).
25. Hegger, H. et al. Pressure-induced superconductivity in quasi-2D $CeRhIn_5$. *Phys. Rev. Lett.* **84**, 4986 (2000).
26. Shishido, H., Settai, R., Harima, H. & Ōnuki, Y. A drastic change of the Fermi surface at a critical pressure in $CeRhIn_5$: dHvA study under pressure. *J. Phys. Soc. Jpn.* **74**, 1103 (2005).
27. Knebel, G., Brison, D. J. P. & Flouquet, J. The quantum critical point in $CeRhIn_5$: a resistivity study. *J. Phys. Soc. Jpn.* **77**, 114704 (2008).
28. Ronning, F. et al. Pressure study of quantum criticality in $CeCoIn_5$. *Phys. Rev. B* **73**, 064519 (2006).
29. Paglione, J. et al. Field-induced quantum critical point in $CeCoIn_5$. *Phys. Rev. Lett.* **91**, 246405 (2003).
30. Norman, M. R. The challenge of unconventional superconductivity. *Science* **332**, 196 (2011).
31. Yuan, H. Q. et al. Observation of two distinct superconducting phases in $CeCu_2Si_2$. *Science* **302**, 2104 (2003).
32. Friedemann, S. et al. Detaching the antiferromagnetic quantum critical point from the Fermi-surface reconstruction in $YbRh_2Si_2$. *Nat. Phys.* **5**, 465 (2009).
33. Nguyen, D. H. et al. Superconductivity in an extreme strange metal. *Nat. Commun.* **12**, 4341 (2021).
34. Löhneysen, H. V., Rosch, A., Vojta, M. & Wölfle, P. Fermi-liquid instabilities at magnetic quantum phase transitions. *Rev. Mod. Phys.* **79**, 1015 (2007).
35. Sidorov, V. A. et al. Superconductivity and quantum criticality in $CeCoIn_5$. *Phys. Rev. Lett.* **89**, 157004 (2002).
36. Park, T. et al. Unconventional quantum criticality in the pressure-induced heavy-fermion superconductor $CeRhIn_5$. *J. Phys. Condens. Mater.* **23**, 094218 (2011).
37. Steglich, F. Evidence of a Kondo destroying quantum critical point in $YbRh_2Si_2$. *J. Phys. Soc. Jpn.* **83**, 061001 (2014).
38. Zhao, H. C. et al. Quantum-critical phase from frustrated magnetism in a strongly correlated metal. *Nat. Phys.* **15**, 1261 (2019).
39. Turkel, S. et al. Nodal hybridization in a two-dimensional heavy-fermion material. *Nat. Phys.* **21**, 1949–1956 (2025).
40. Miclea, C. F. et al. Pressure dependence of the Fulde–Ferrell–Larkin–Ovchinnikov state in $CeCoIn_5$. *Phys. Rev. Lett.* **96**, 117001 (2006).
41. Kittaka, S. et al. Thermodynamic study of gap structure and pair-breaking effect by magnetic field in the heavy-fermion superconductor $CeCu_2Si_2$. *Phys. Rev. B* **94**, 054514 (2016).
42. Kimura, N., Ito, K., Aoki, H., Uji, S. & Terashima, T. Extremely high upper critical magnetic field of the noncentrosymmetric heavy fermion superconductor $CeRhSi_3$. *Phys. Rev. Lett.* **98**, 197001 (2007).

43. Khim, S. et al. Field-induced transition within the superconducting state of $CeRh_2As_2$. *Science* **373**, 1012 (2021).
44. Squire, O. P. et al. Superconductivity beyond the conventional Pauli limit in high-pressure $CeSb_2$. *Phys. Rev. Lett.* **131**, 026001 (2023).
45. Schossmann, M. & Carbotte, J. P. Pauli limiting of the upper critical magnetic field. *Phys. Rev. B* **39**, 4210 (1989).
46. Thomas, F. et al. Strong coupling effects on the upper critical field of the heavy-fermion superconductor UBe_{13}. *J. Low Temp. Phys.* **102**, 117 (1996).
47. Bauer, E. & Sigrist, M. Non-centrosymmetric superconductors: introduction and overview. In *Lecture Notes in Physics* Vol. 847, 192–209 (Springer, 2012).

Methods

Crystal growth and characterizations

CeSiI single crystals were grown by a high-temperature-solid-state reaction as described in refs. 10,11. The handling of the elements and compounds was all performed in an argon-filled glovebox. CeI_3 was first prepared by reaction of stoichiometric amounts of Ce and I_2 at 1,000 °C for 3 days. Then, the Ce pieces (99.95% purity from Zhong Nuo Advanced Material (Beijing) Technology), Si powder (99.95% purity from Zhong Nuo Advanced Material (Beijing) Technology) and the synthesized CeI_3 powder with a molar ratio of 2:3:1 were put into the Ta tube, which was sealed using the arc melting method in an argon atmosphere. The Ta tube was subsequently sealed into a quartz tube under vacuum, before finally being placed into a box furnace. The furnace temperature was raised slowly to 1,273 K for 1 day and then held for another 6 days. After that, the furnace was slowly cooled down to 973 K at the rate of 3 K h^{-1} and then turned off. Shiny, black plate-like hexagonal crystals with the lateral dimensions up to 2 mm can be obtained from the growth. The CeSiI single crystals are sensitive to air and moisture and thus are stored in an Ar-filled glovebox to avoid degradation. Detailed characterizations of CeSiI single crystals are shown in Extended Data Fig. 1. The energy-dispersive X-ray spectroscopy, which confirms that it contains three elements Ce, Si and I with the average molar ratio close to 0.97(5):1.03(1):1, which is close the chemical formula of CeSiI.

High-pressure transport measurements

Temperature-dependent resistivity $\rho(T)$ under various pressures up to 14 GPa was measured using a standard four-probe configuration in a palm-type cubic anvil cell apparatus[48,49], which can generate excellent hydrostatic pressures due to three-axis compression geometry and the adoption of liquid pressure transmitting medium. The electrical current was applied within the *ab* plane and the external magnetic field was applied parallel to the *c* axis. The pressure values in the cubic anvil cell were estimated from the calibration curve predetermined via monitoring structural transitions of bismuth (Bi) and tin (Sn) metals at room temperature[49]. The low-temperature measurements were carried out in a ^{4}He exchange-gas cryostat (down to 1.5 K) or a dilution refrigerator cryostat (down to 0.05 K) equipped with a 12 T superconducting magnet at the Synergic Extreme Condition User Facility.

Data availability

The data supporting the findings of this study are available via the MatELab at https://matelab.iphy.ac.cn/eln/link.html#/191/L3j0. Additional data are available from the corresponding authors upon reasonable request.

References

48. Uwatoko, Y. et al. Development of palm cubic anvil apparatus for low temperature physics. *Rev. High Press. Sci. Tech.* **18**, 230 (2008).
49. Cheng, J.-G. et al. Integrated-fin gasket for palm cubic-anvil high pressure apparatus. *Rev. Sci. Instrum* **85**, 093907 (2014).

Acknowledgements

We acknowledge support from the Cubic Anvil Cell station of Synergetic Extreme Condition User Facility (SECUF, https://cstr.cn/31123.02.SECUF) for the high-pressure measurements.

Author contributions

J.C., B.W. and H.L. supervised this project. W.L. and H.L. synthesized the CeSiI single crystals and characterized their crystal structure and physical properties at ambient pressure; T.S., Q.D., B.W. and J.C. performed resistivity and a.c. magnetic susceptibility measurements at high pressures using the cubic anvil cell apparatus with the support of P.Y., H.M., Z.T., N.W., J.S. and Y.U.; Y.Y. gave important advice from a theoretical perspective; J.C., B.W., Y.Y. and H.L. wrote the paper with inputs from all authors.

Funding

This work was supported by the National Key Research and Development Program of China (grant nos. 2023YFA1406100 to J.C., 2024YFA1408400 to B.W., 2023YFA1607400 to B.W., 2023YFA1406500 to H.L., 2022YFA1403800 to H.L. and 2022YFA1402203 to Y.Y.), the National Natural Science Foundation of China (grant nos. 12025408 to J.C., 12474055 to B.W., 12174424 to J.S., 12522407 to J.S., 12404067 to P.Y., U23A6003 to J.C., 12274459 to H.L. and 12474136 to Y.Y.), the CAS President's International Fellowship Initiative (grant no. 2024PG0003 to Y.U.), the Outstanding Member of Youth Promotion Association of CAS (grant no. Y2022004 to B.W.) and the CAS Superconducting Research Project (grant no. SCZX-0101 to P.Y. and J.C.). Part of this work was supported by JSPS KAKENHI 25K00951 to Y.U.

Competing interests

The authors declare no competing interests.

Additional information

Extended data is available for this paper at https://doi.org/10.1038/s41567-026-03392-3.

Supplementary information The online version contains supplementary material available at https://doi.org/10.1038/s41567-026-03392-3.

Correspondence and requests for materials should be addressed to Yi-feng Yang, Bosen Wang, Hechang Lei or Jinguang Cheng.

Peer review information *Nature Physics* thanks the anonymous reviewer(s) for their contribution to the peer review of this work.

https://doi.org/10.1038/s41567-026-03392-3

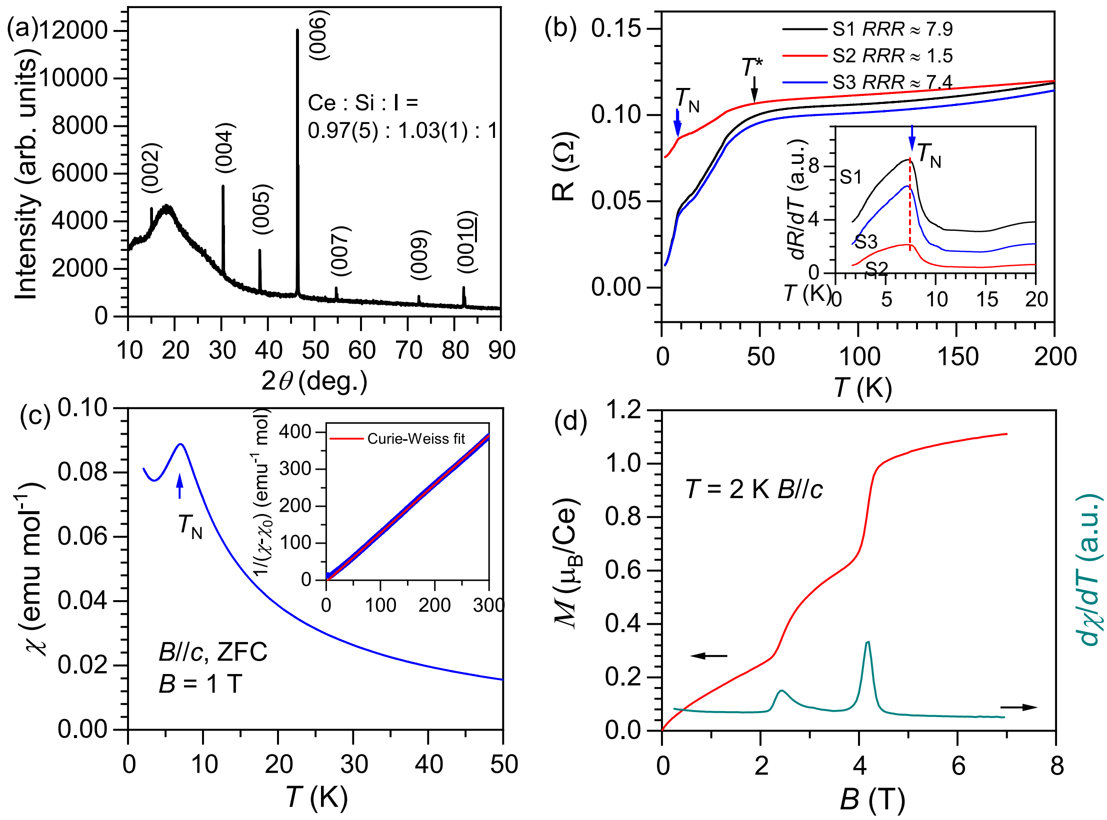

Extended Data Fig. 1 | Single crystal X-ray diffraction, electrical transport and magnetic properties of CeSiI at ambient pressure. (**a**) X-ray diffraction pattern of a CeSiI single crystal measured at room temperature covered with Kapton tape, which produces a hump centered at ~20 degree. All peaks can be indexed by the indices of (00 *l*) planes, confirming the *c*-axis perpendicular to the crystal surface. The energy-dispersive X-ray spectroscopy yields the atomic ratio of Ce: Si: I = 0.97(5): 1.03(1): 1 when setting the content of I as 1, close to the chemical formula of CeSiI. (**b**) Electrical resistivity $\rho(T)$ of CeSiI at ambient pressure (AP) for three samples S1, S2 and S3. They show similar major features and slight sample dependency. The residual resistivity ratio, $RRR \equiv \rho(T^*)/\rho(1.6\text{ K})$, are 7.9 (7.3) for S1 (S3) and 1.5 for S2 at AP, which increases to 14.75 for S1 and 3.54 for S2 at 2 GPa, respectively [Extended Data Fig. 4(c)]. (**c**) Magnetic susceptibility $\chi(T)$ with an applied magnetic field of $B = 1$ T parallel to the *c* axis under a zero-field-cooling (ZFC) process. The Néel temperature $T_N = 7.1$ K can be determined from the cusp of $\chi(T)$. The inset shows the Curie-Weiss fitting to the high-temperature paramagnetic region (red line) with $C = 0.76$ (9) emu K mol^{-1} ($\mu_{eff} = 2.47$ (1) μ_B/f.u.) and $\theta = -3.12$ (6) K. The former is close to the magnetic moment of Ce^{3+} ion, that is $\mu_{eff} = 2.54\ \mu_B$. (**d**) Field dependence of magnetization $M(T)$ at 2 K for $B // c$. There are two successive metamagnetic transitions at $B \approx 2.4$ and 4.1 T, respectively, reflected as a peak in dM/dT. The saturation moment at 7 T is about 1.11 μ_B/f.u.

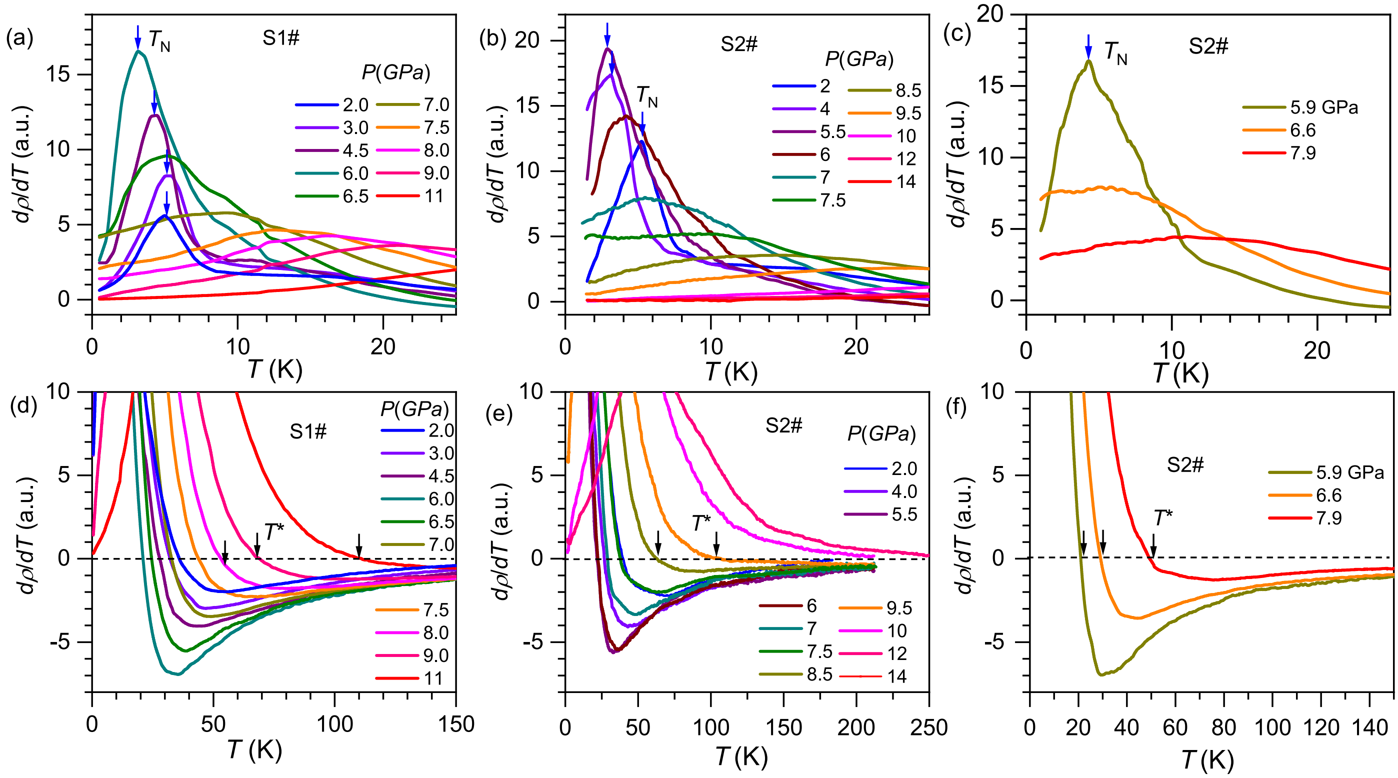

Extended Data Fig. 2 | The characteristic temperatures T_N and T* of CeSiI determined from temperature-derivative of resistivity d*ρ*/d*T*. Temperature dependences of $d\rho/dT$ for (**a, e**) S1 and (**b, d**) S2 under various pressures measured upon compression, and (**c, f**) S2 measured during decompression. T_N marked by the kink anomaly in $\rho(T)$ corresponds to the peak of $d\rho/dT$, and T^* manifested as the hump in $\rho(T)$ is defined as the temperature at which the $d\rho/dT$ crosses zero, respectively. The black and blue arrows represent the T^* and T_N, respectively.

 https://doi.org/10.1038/s41567-026-03392-3

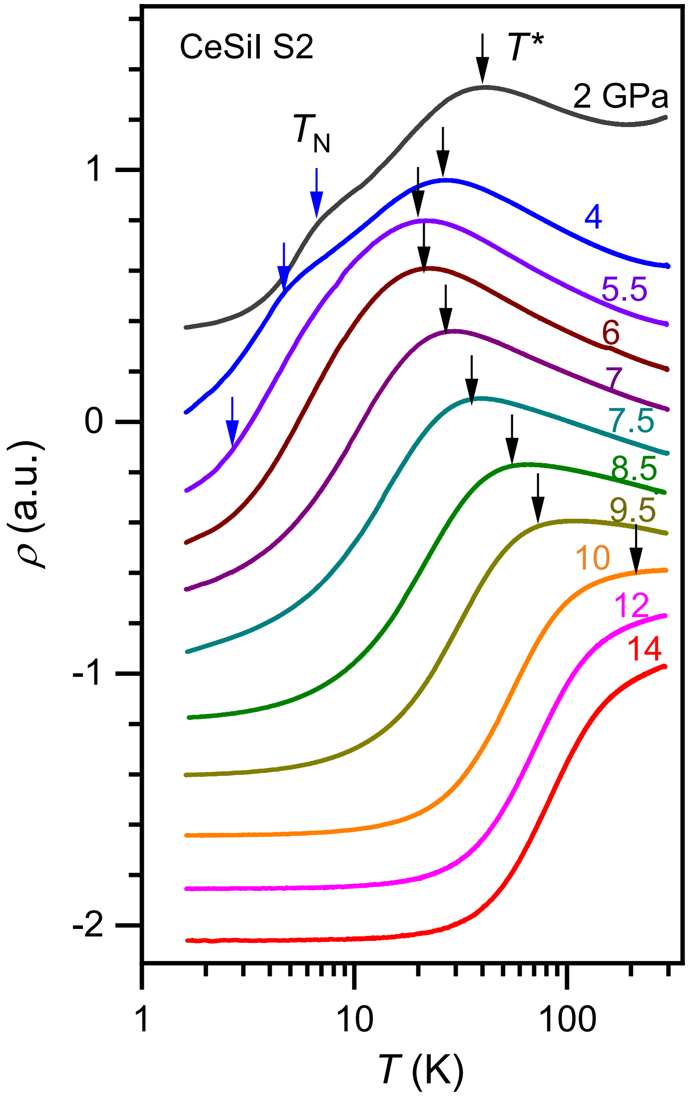

Extended Data Fig. 3 | High-pressure resistivity of CeSiI S2 measured in a ^{4}He cryostat. The $\rho(T)$ of CeSiI (S2) under various pressures upon compression from 2 to 14 GPa measured in a ^{4}He cryostat from 1.5 to 300 K. All $\rho(T)$ curves except that at 2 GPa are shifted vertically for clarity. The black and blue arrows indicate the characteristic temperatures T^* and T_N, respectively.

 https://doi.org/10.1038/s41567-026-03392-3

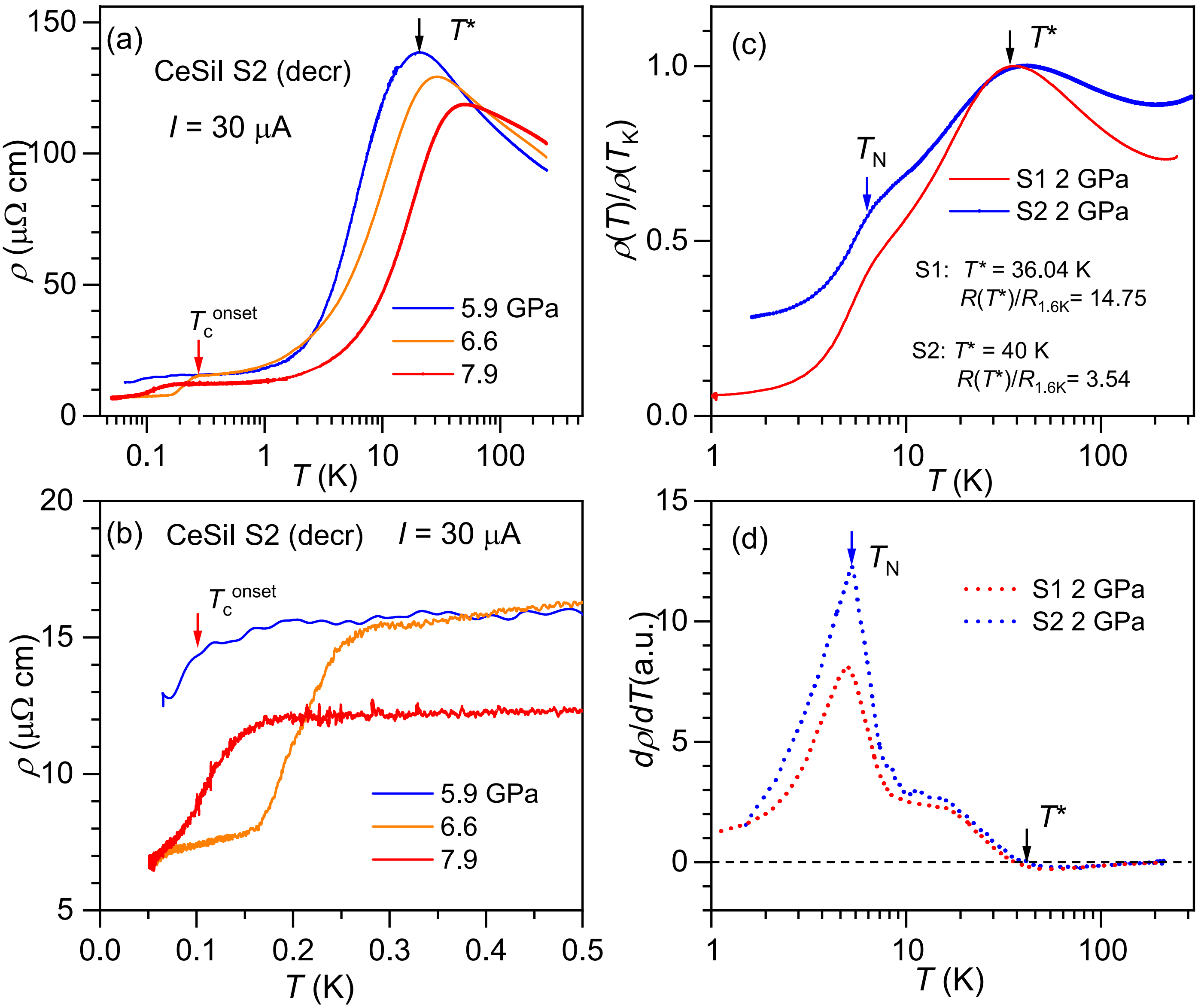

Extended Data Fig. 4 | The resistivity of CeSiI S2 measured in a dilution refrigerator during decompression. (**a**) The $\rho(T)$ of CeSiI (S2) measured at low temperatures of 50 mK-40 K under various pressures during decompression from 7.9 to 5.9 GPa. (**b**) The enlarged view of $\rho(T)$ data below 0.5 K. (**c**) The normalized $\rho(T)/\rho(T^*)$ of CeSiI (S1, S2) at a fixed pressure of 2 GPa to compare the residual resistivity ratio, that is, $RRR = \rho(T^*)/\rho(1.6\ \mathrm{K})$, of these two samples. (**d**) The $d\rho/dT$ of CeSiI (S1, S2) at 2 GPa. The black and blue arrows represent the T^* and T_N, respectively.

https://doi.org/10.1038/s41567-026-03392-3

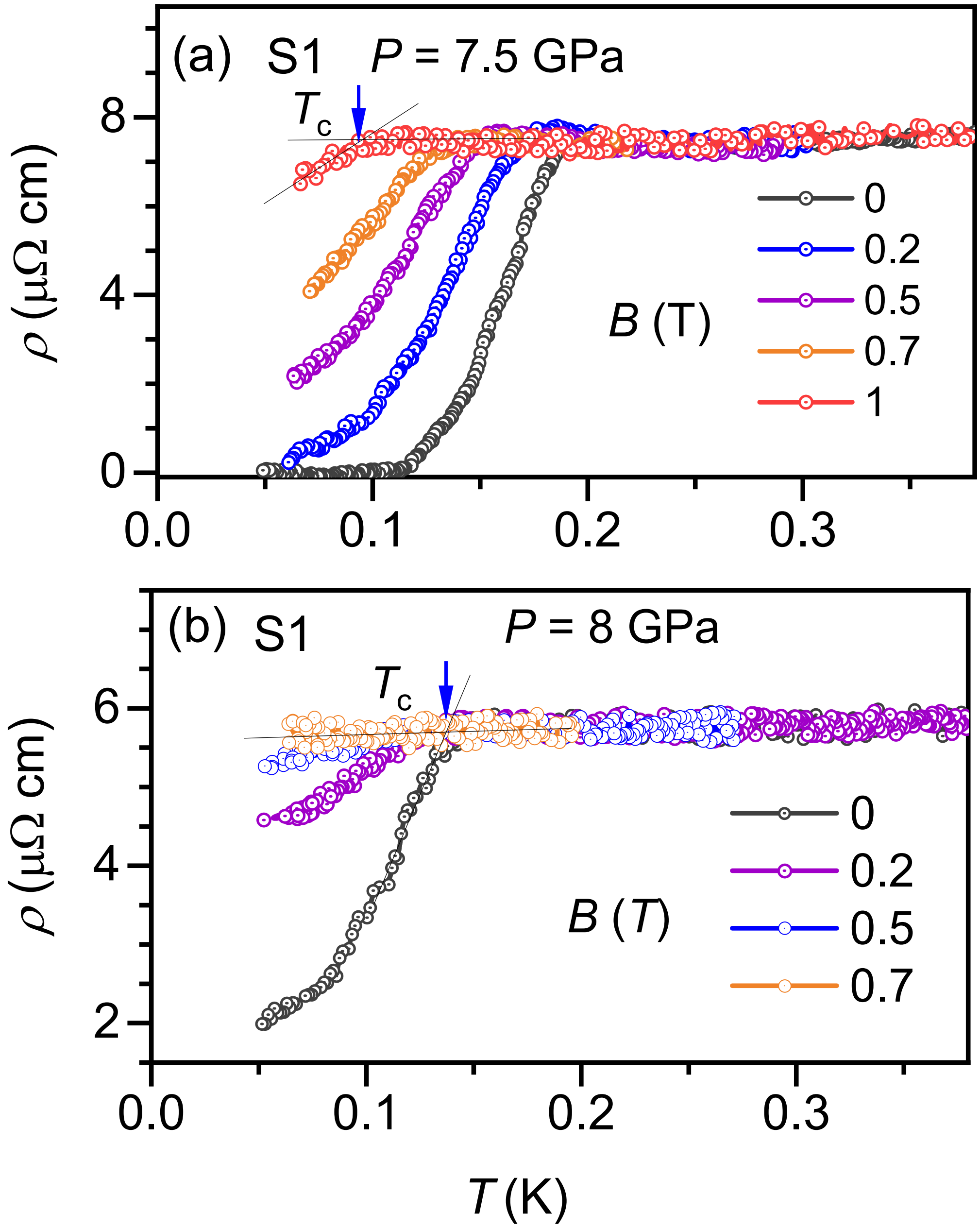

Extended Data Fig. 5 | Effect of magnetic field on the superconducting transition of CeSiI. Low-T $\rho(T)$ of CeSiI (S1) under various magnetic fields for different pressures: (**a**) P = 7.5 GPa, 0-1 T; (**b**) P = 8 GP, 0-0.7 T. The onset of superconducting transition temperature T_c was determined by the intersection of two straight lines as shown in (**a**).

 https://doi.org/10.1038/s41567-026-03392-3

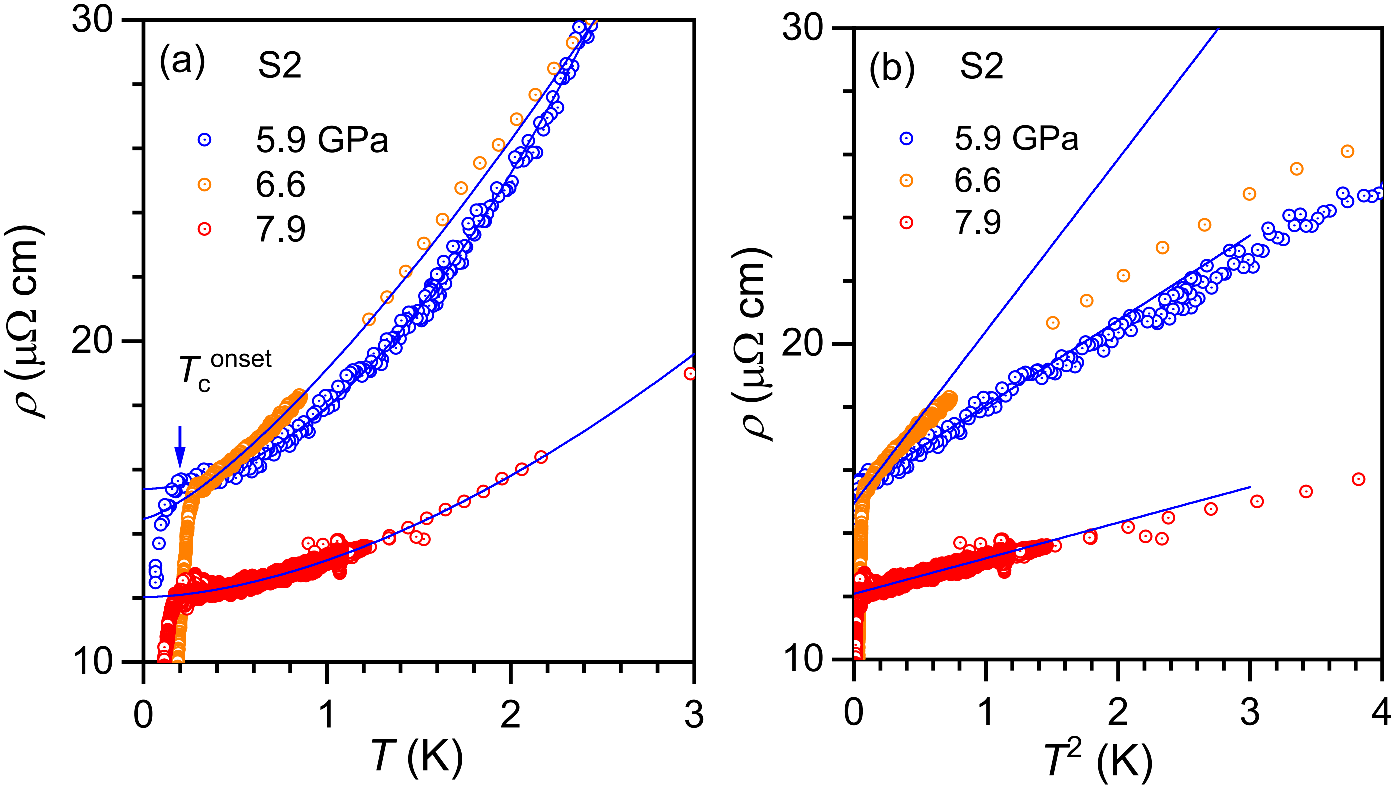

Extended Data Fig. 6 | Power-law fitting to low-temperature resistivity of CeSiI S2. (**a**) Power-law fitting to low-T $\rho(T)$ by using $\rho(T) = \rho_0 + A'T^n$ for CeSiI (S2). (**b**) The T-quadratic fitting to low-T $\rho(T)$ by using $\rho(T) = \rho_0 + AT^2$ for CeSiI (S2). All the solid lines indicate the fitting results.